nature materials

ARTICLES

https://doi.org/10.1038/s41563-021-01017-z

Check for updates

Tension–compression asymmetry in amorphous silicon

Yuecun Wang[1,6], Jun Ding[2,6], Zhao Fan[3,6], Lin Tian[4,6], Meng Li[1], Huanhuan Lu[1], Yongqiang Zhang[1], En Ma[2]✉, Ju Li[5]✉ and Zhiwei Shan[1]✉

Hard and brittle materials usually exhibit a much lower strength when loaded in tension than in compression. However, this common-sense behaviour may not be intrinsic to these materials, but arises from their higher flaw sensitivity to tensile loading. Here, we demonstrate a reversed and unusually pronounced tension–compression asymmetry (tensile strength exceeds compressive strength by a large margin) in submicrometre-sized samples of isotropic amorphous silicon. The abnormal asymmetry in the yield strength and anelasticity originates from the reduction in shear modulus and the densification of the shear-activated configuration under compression, altering the magnitude of the activation energy barrier for elementary shear events in amorphous Si. In situ coupled electrical tests corroborate that compressive strains indeed cause increased atomic coordination (metallization) by transforming some local structures from sp^3-bonded semiconducting motifs to more metallic-like sites, lending credence to the mechanism we propose. This finding opens up an unexplored regime of intrinsic tension–compression asymmetry in materials.

Inorganic materials with covalent or ionic bonding are well known to be much stronger in compression than in tension. That is, for a given material, the experimentally recorded compressive strength (σ_C) is usually much higher than the tensile strength (σ_T)[1–3]. However, this apparent tension–compression (T-C) asymmetry is not the intrinsic inelastic response of these materials, but instead originates from the very different sensitivity to preexisting flaws (such as the internal voids, pores and surface blemishes)[4,5] under tension versus compression. Specifically, a tensile load tends to open up the flaw into an incipient crack and accelerate the crack propagation, such that fracture sets in prematurely at relatively low stresses to preempt global yielding[6]. By contrast, flaws tend to close up under a compressive load, such that the compressive yield strength is much higher and close to the intrinsic strength of the material[3]. A fundamental question then naturally arises, as to whether a T-C asymmetry remains when the effects of flaws are eliminated, and if it does, would σ_C be higher or lower than σ_T, by how much and why.

To answer the question posed above, we resort to samples that are initially nearly free of extended defects[7], such that the chances for premature fracture are minimized[8,9]. One known way to do this is to reduce the physical dimensions of the tested volume, as ultrahigh strength close to the theoretical limit has been demonstrated before in micro- and nano-scale samples[8,10]. We, therefore, carried out quantitative compression versus tension testing of submicrometre-sized amorphous Si (a-Si), feasible using a nanomechanical testing system inside a transition electron microscope (TEM). Here the choice of a-Si is made, in lieu of crystalline compounds, to avoid complications due to variable slip systems, crystal anisotropy and chemical composition, not to mention that a-Si is one of the most important semiconductors and a classic model material for the fundamental research of disordered matter[11–15]. In the following, we will demonstrate an unusual T-C asymmetry: the $\sigma_C >> \sigma_T$ norm is reversed, and astonishingly σ_T exceeds σ_C by a large margin. This surprising observation is also corroborated in atomistic simulations.

Results

T-C asymmetry in submicrometre-sized a-Si. Submicrometre-sized a-Si samples, micromachined from deposited a-Si film (Supplementary Fig. 1) using a focused ion beam (FIB), were tested in both tension and compression. One type of test used the same specimen for tension and compression, thus excluding possible artefacts from comparing different samples. This type of tensile-compressive (TC) sample is shown in Fig. 1a. The TC sample was first subjected to tensile loading. The gauge section elongated with increased loading, and then fractured abruptly (Fig. 1a). After the tensile fracture, the lower half of the TC sample remained intact, with its flat fracture surface perpendicular to the loading direction (Fig. 1b). This part of the sample was then used for compression, loaded under a flat diamond punch. In compression, the sample showed continuous shape change with homogeneous plastic flow after yielding. Supplementary Video 1 shows the real-time tensile and compressive deformation processes. The corresponding engineering stress–strain curve is presented in Fig. 1c (effective size, $d = 145$ nm). The flow stress at a 5% plastic strain, ~4.5 GPa for this sample, is taken as the yield strength in compression. In tension, however, a-Si did not yield at stresses exceeding ~4.5 GPa, until the fracture set in at ~6.5 GPa. It is uncertain if this fracture is preceded by yielding, with large but highly localized plastic strains that have immediately instigated failure. Another possibility is that the sudden fracture may be triggered prematurely by minor flaws in the specimen, preempting yielding. In any case, under tension, the

[1]Center for Advancing Materials Performance from the Nanoscale and Hysitron Applied Research Center in China, State Key Laboratory for Mechanical Behavior of Materials, Xi'an Jiaotong University, Xi'an, China. [2]Center for Alloy Innovation and Design, State Key Laboratory for Mechanical Behavior of Materials, Xi'an Jiaotong University, Xi'an, China. [3]Department of Materials Science and Engineering, Johns Hopkins University, Baltimore, MD, USA. [4]Institute of Materials Physics, University of Göttingen, Niedersachsen, Germany. [5]Department of Nuclear Science and Engineering, Department of Materials Science and Engineering, Massachusetts Institute of Technology, Cambridge, MA, USA. [6]These authors contributed equally: Yuecun Wang, Jun Ding, Zhao Fan, Lin Tian. ✉e-mail: maen@xjtu.edu.cn; liju@mit.edu; zwshan@xjtu.edu.cn

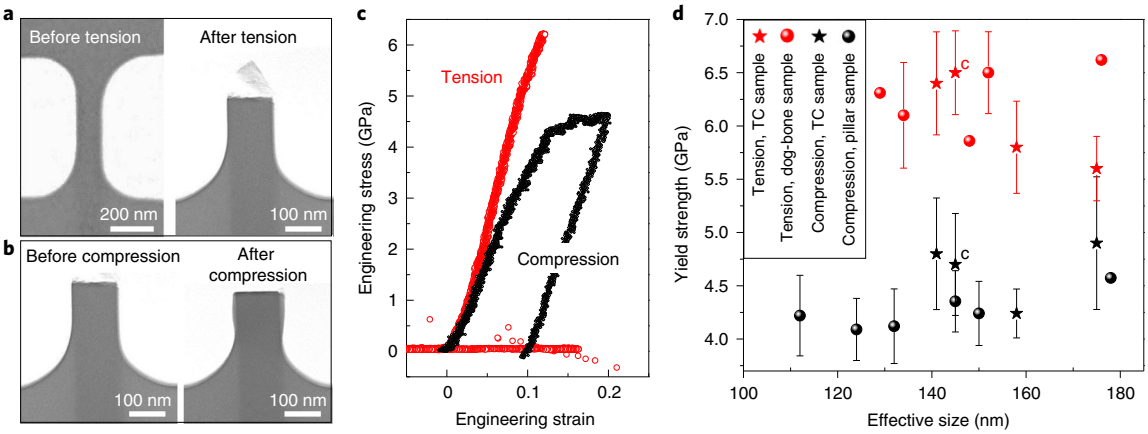

Fig. 1 | T-C asymmetry in submicrometre-sized a-Si. a, The gauge section of a typical TC a-Si sample before the test (left) and after its brittle fracture in the tensile test (right). **b**, Subsequent compression test on the leftover sample section. **c**, Engineering stress–strain curves of the TC sample under tension (red) and compression (black). **d**, Tensile and compressive yield strength of a-Si samples with the effective size of ~110–180 nm. The 'c' labels correspond to the tensile and compressive curves in **c**. The error bar encloses twice the standard deviation.

stress needed to induce yielding is at least ~6.5 GPa, which is designated as the 'yield strength' in tension.

One may wonder if this asymmetry is due to tension-induced fertile sites for shear transformations[16], causing some softening in the subsequent compression. Therefore, we also prepared independent tensile and compression samples, that is, separate pillars for compression and 'dog-bone shaped' samples for tension (Methods). For these samples, the measured strengths follow the same trend as that in TC samples: tensile excursion ends in fracture while compressive loading initiates homogeneous plastic flow at a much lower stress level (more data are documented in Supplementary Fig. 2). Figure 1d summarizes the yield strength of a-Si (d = ~110–180 nm) under compression (black) versus that under tension (red). We see that σ_T is considerably higher than σ_C. In other words, we consistently observe that a-Si is much stronger in tension than in compression. Note that a-Si remained fully amorphous after either tensile or compressive deformation, as confirmed in post-mortem characterizations (Supplementary Fig. 3).

Dynamic tests in the apparent elastic regime provide further insight into the T-C asymmetry of a-Si. To achieve high sensitivity, we used the nano dynamic mechanical analysis technique[17,18]. Stress–displacement curves were obtained by overlapping ten loading–unloading cycles with peak stress well below the yielding strength. In the dynamic tensile tests, a-Si exhibits a linear elastic behaviour for loading frequencies ranging from 0.5 Hz to 20 Hz (Fig. 2a). The push-to-pull device itself, in the absence of an a-Si sample, also showed perfect linear elasticity (Supplementary Fig. 4). By contrast, the compressed a-Si exhibits a mechanical hysteresis loop, which expands gradually with increasing loading frequency. The energy dissipated can be assessed using the damping factor, which represents the ratio of the loss modulus to the storage modulus[19]. Storage modulus is a metric for the elastic energy stored in the sample; loss modulus, on the other hand, is a gauge of viscous response and measures the energy dissipated as heat[20]. In compression, the damping factor is found to be 0.009, 0.044, 0.105, 0.098 and 0.162, corresponding to the average strain rate of 0.05 s^{-1}, 0.20 s^{-1}, 0.51 s^{-1}, 0.95 s^{-1} and 1.82 s^{-1}, respectively. Comparing tension versus compression in the nominally elastic regime, apparently a-Si is more elastic and stores more elastic strain energy under tension, whereas it undergoes much more anelastic relaxation with energy dissipation in compression. This T-C asymmetry in an elastic-dominant regime, that is, anelasticity, is markedly enhanced under compression but suppressed under tension, and goes hand in hand with the asymmetry in yield strength.

Atomistic simulations of the T-C asymmetry in a-Si. To corroborate the experimentally observed T-C asymmetry and shed light on the underlying mechanism, we have carried out molecular dynamics (MD) simulations using three different empirical potentials for a-Si, including the Stillinger–Weber potential[21] and an environment-dependent interatomic potential[22], as well as a newly developed machine-learning (ML) interatomic potential[23], which has been shown to generate atomic structure and properties close to the experimental measurements[24]. All these empirical potentials are consistent in producing the T-C asymmetry. For conciseness, in the main text we only show the ML potential simulation results, whereas the results of the Stillinger–Weber and environment-dependent interatomic potentials are documented in the Supplementary Information and Methods with details about model preparation and deformation simulation.

We first simulated the uniaxial compression and tension of a-Si, in which the applied uniaxial load can be decomposed into shear stress τ and normal stress σ_n on the maximum shear plane (inclined ~45° to the loading axis), as schematically illustrated in Fig. 3a. The compressive yielding required a stress of ~5.5 GPa at a strain of ~9%, while the tensile yield strength is 7.2 GPa at a strain of 13% (Fig. 3b). Such a T-C asymmetry ($\sigma_C < \sigma_T$; also Supplementary Figs. 5 and 6) is consistent with the experimental results in Fig. 1. The uniaxial tension and compression correspond to, respectively, positive (that is, $\sigma_n > 0$) and negative (that is, $\sigma_n < 0$) normal stress; the normal stress effect is therefore the key factor responsible for the T-C asymmetry. To provide quantitative information about the σ_n effect and remove the influence of the free surface, we consider a deformation model of simple shear concurrent with a constant perpendicular normal stress σ_n (as illustrated in the right panel of Fig. 3a). Figure 3c presents the shear stress–strain curves for ML a-Si in three σ_n cases (0 GPa, 3.5 GPa and −3.5 GPa). We observe that $\sigma_n < 0$ leads to lowered yield strength, while $\sigma_n > 0$ leads to increased yield strength, in agreement with the results presented earlier.

Next, we employed MD simulations to calculate the shear modulus G of a-Si at 300 K under different σ_n applied along the z axis. G is examined here mainly because it is widely regarded as a key baseline property for amorphous materials, and known to be closely related to the energy barrier for shear transformation, yielding/flow

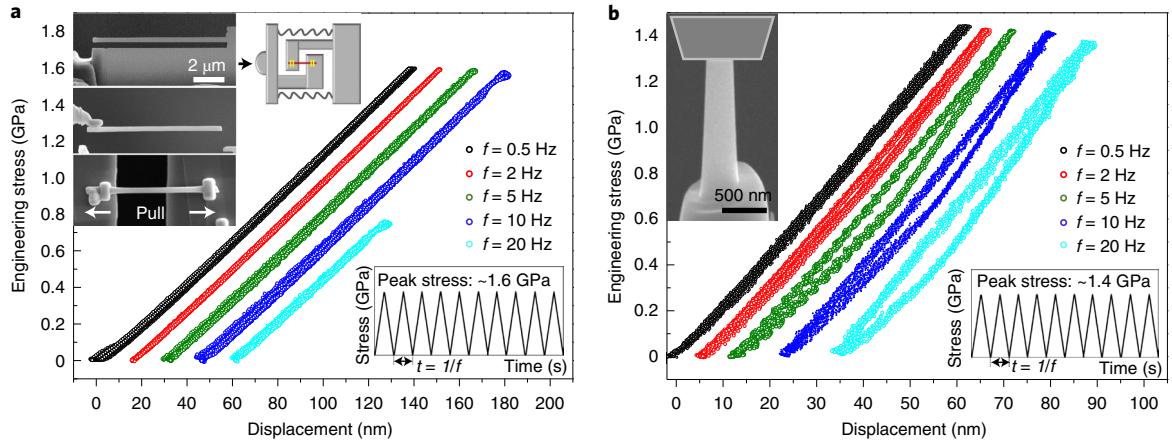

Fig. 2 | T-C asymmetry of submicrometre-sized a-Si in the nominally 'elastic' regime. a, The load–displacement curves obtained by cycling an a-Si tensile sample ten times at different load–unload frequencies (*f*, the number of loading–unloading cycles per second). The left insets show that the a-Si tensile sample was thinned and cut by FIB, transferred to a push-to-pull device and then fixed using Pt deposition on both ends. The lower right corner inset shows the triangular-shaped loading cycles, consisting of symmetrical loading and unloading portions (*t*, the reciprocal of *f*, represents the period time of a loading–unloading cycle). **b**, The load–displacement curves obtained by cycling an a-Si pillar under compression ten times at different load cycle frequencies. The upper left inset shows the scanning electron microscopy image of the pillar after the test. The lower right corner inset shows the triangular-shaped loading cycles.

and structural relaxation, as shown, for example, in the cooperative shear model developed by Johnson and Samwer[25]. Figure 3d shows the change of G_{xz} (or G_{yz}) and G_{xy} as strain increases. Here the first and second subscript of G_{ij} represent the shear direction and normal direction of the shear plane, respectively (therefore G_{yz} is identical to G_{xz} considering the applied σ_n is along the *z* axis). Since G_{xz} and G_{yz} are shear moduli in the plane normal to σ_n, they determine the energy barrier for shear events, under the tension or compression along the *z* axis (resembling the uniaxial deformation illustrated in Fig. 3a). In early stages of straining, tensile normal stress ($\sigma_n > 0$) increases G_{xz} (or G_{yz}), which goes through a maximum value at large strains. By contrast, under compressive normal stress ($\sigma_n < 0$), G_{xz} (or G_{yz}) keeps decreasing from the start. The evolution of G_{xy} exhibits an opposite trend compared with G_{xz} and G_{yz}: the tensile normal stress leads to lower G_{xy}, while compressive stress increases G_{xy} slightly first and then reduces it. Therefore, the shear moduli become anisotropic when a normal stress is imposed on a-Si. This anisotropic variation/response of shear moduli, in turn, is partly responsible for the T-C asymmetry we have observed (more explanations are in the Discussions section). The fourfold sp^3-bonded tetrahedra are the dominant local coordination motifs in a-Si (Supplementary Fig. 7). The analysis of orientational radial distribution function[26] (Supplementary Fig. 8) demonstrates that under tension and compression, the main structural change for those Si tetrahedra is the bonding anisotropy (as depicted by the elongated and shortened tetrahedra in Fig. 3e). As such, the normal-stress-sign-dependent response of shear moduli can be mainly attributed to this bonding anisotropy.

Besides shear modulus, we also take the coordination number (CN) change into consideration. An analysis of the fraction of a-Si atoms with CN = 4 and CN > 4 (Supplementary Fig. 7) shows that most atoms (over 90%) remain tetrahedral during deformation. The increase in the fraction of atoms with CN > 4 is associated with deformation-induced fertile sites for shear transformations[16,27], and the increased CN > 4 sites under compression is higher than that under tension, especially in the plastic deformation regime, suggesting that compressive stress is more inclined to facilitate the local transformation from tetrahedral atomic environments to higher-coordinated, more fertile sites. Specifically, our deformation simulations under athermal quasi-static conditions, in which the influence from thermal noise is absent, show that the fraction of Si atoms with non-affine squared displacement (D^2_{min}) > 1×10^{-4} Å^2 (calculated with a constant strain offset of 0.01%) under compression is about twice that under tension (for example, ~3.1% versus ~1.5% for tension and compression at the elastic strain of 0.02). This accounts for the T-C asymmetry in terms of anelasticity, since the origin of the nonlinear elasticity of amorphous solids rests in the liquid-like non-affine deformations[28]. We can also unify the anisotropic shear moduli at different normal stresses (in both elastic and plastic regimes) by identifying a single structural parameter λ_{ij}, where *i* and *j* are in the set of *x*, *y* or *z* directions. See Supplementary Note 1 and Supplementary Figs. 9–11 for details.

T-C asymmetry probed via resistance change. To verify the prediction about the CN change using simulations, we further carried out in situ coupled mechanical–electrical tests inside a TEM to measure the real-time electrical resistances of a-Si under tension and compression. If the shear deformations that locally convert the covalently bonded and semiconducting tetrahedral environments into more metallic fertile motifs with CN > 4 (refs. [27,29,30]) are suppressed in tension but facilitated in compression, the resistivity change is expected to be different in tension and compression.

Figure 4a shows the resistance change with time for a typical a-Si sample under tensile stress. Because the samples were loaded under a constant strain rate, the strain incurred is proportional to time under loading. The grey dashed line in Fig. 4a shows the calculated resistance change due to geometry change (Supplementary Note 2, Supplementary Figs. 12 and 13 and Supplementary Table 1 for calculation details). The curve agrees well with the measured resistance, indicating that the observed resistance increase during tensile deformation arises entirely from sample elongation, and the resistivity stays constant. For compression, by contrast, the grey dashed curve shows the resistance reduction induced by the pure geometry change of the a-Si pillar during the compressive flow and does not agree with the measured resistance change (Fig. 4b). The difference between them, especially in the plastic deformation stage, indicates that the resistivity of a-Si decreased under compression. Such an observation is consistent with, and lends support to, the mechanism revealed by atomistic

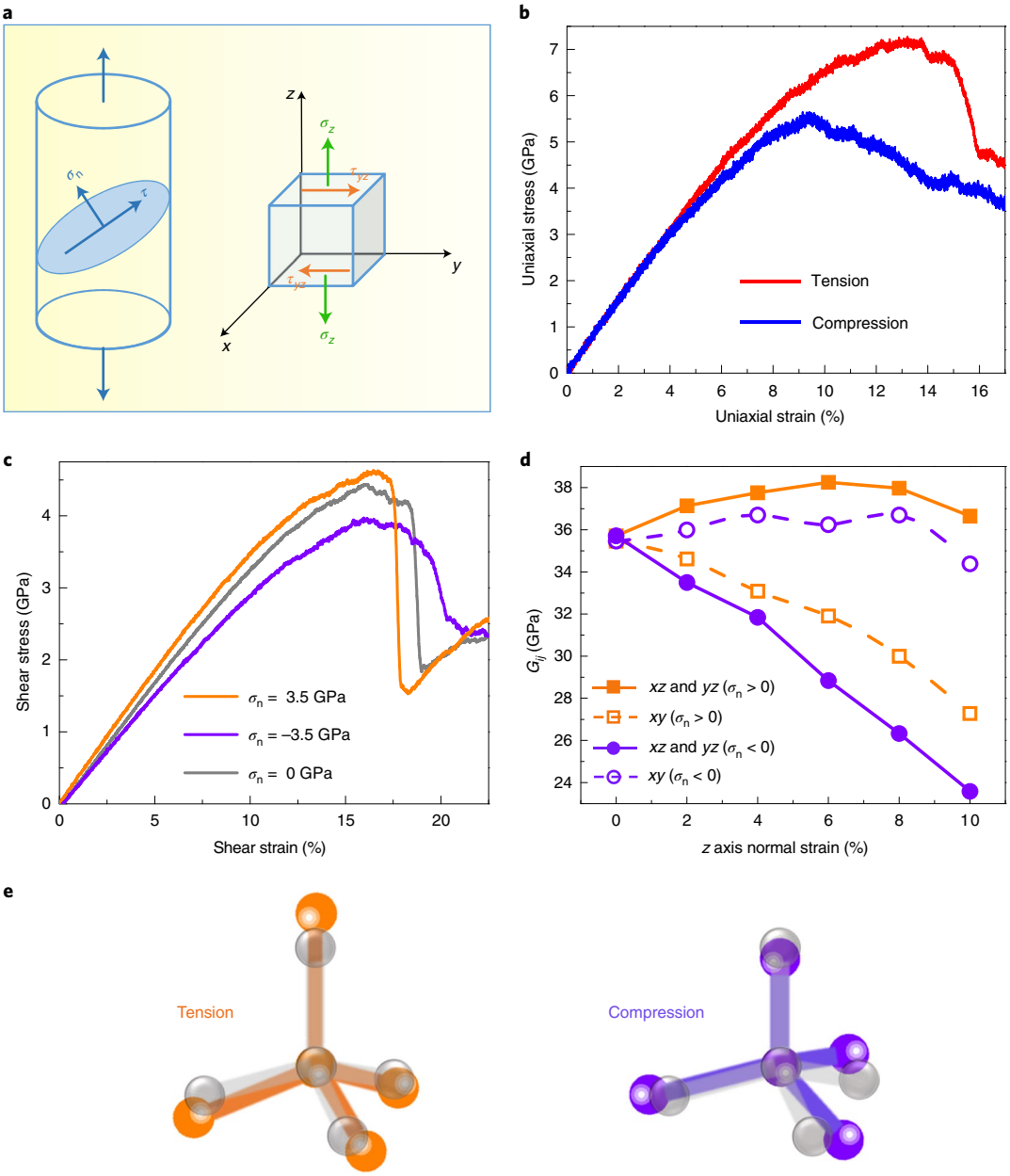

Fig. 3 | MD simulations of the T-C asymmetry in a-Si. a, Schematic showing uniaxial deformation (left) as well as simple shear deformation with simultaneously imposed perpendicular normal stress (right). **b**, Stress–strain curves of uniaxial tension and compression along the *z* axis at 300 K for a ML a-Si model with free surface in the *x* direction (periodic boundary conditions in the *y* and *z* directions). **c**, Stress–strain curves for simple shear deformation on the *xy* shear plane in the *x* direction, simultaneously with applied normal stress σ_n, as illustrated in **a**, of a ML a-Si model (periodic boundary conditions in all three dimensions). **d**, Effects of normal stress (σ_n in the *z* direction) on the shear moduli G_{xz} (and G_{yz}) and G_{xy} of ML a-Si at 300 K. **e**, Typical relative rearrangements of the tetrahedral packing under tension and compression. The a-Si tetrahedron in grey is its unstrained state. Under tension (compression), bonds parallel to *z* axis stretched (contracted), while bonds perpendicular to the *z* axis contracted (stretched).

simulations (Fig. 3). That is, compressive normal stress serves to enhance the propensity for shear transformation events, which transform the semiconducting 'solid-like' atomic environments into more metallic (conductive) and denser ones, decreasing the resistivity as a result. We also obtained evidence that shear transformations have indeed increased density (Supplementary Note 3 and Supplementary Fig. 14). By contrast, tension suppresses shear transformations, such that the sample experiences mainly elastic deformation, without producing many metallic and denser environments. This is manifested by the negligible change in resistivity demonstrated in Fig. 4a.

Discussions

Our results, both experimental and computational, have shown two major contributing factors to the extraordinary T-C asymmetry in a-Si. The first is the changes in the shear moduli, that is, stiffening versus weakening, depending on the sign of the normal stress. This contribution comes into play even in the nominally elastic regime, as compression lowers the shear modulus and consequently the barrier against non-affine shear transformations that produce pronounced anelasticity. The other contribution is shear-transformation-induced densification or 'liquefaction', which converts local packing motifs into denser and more metallic-like

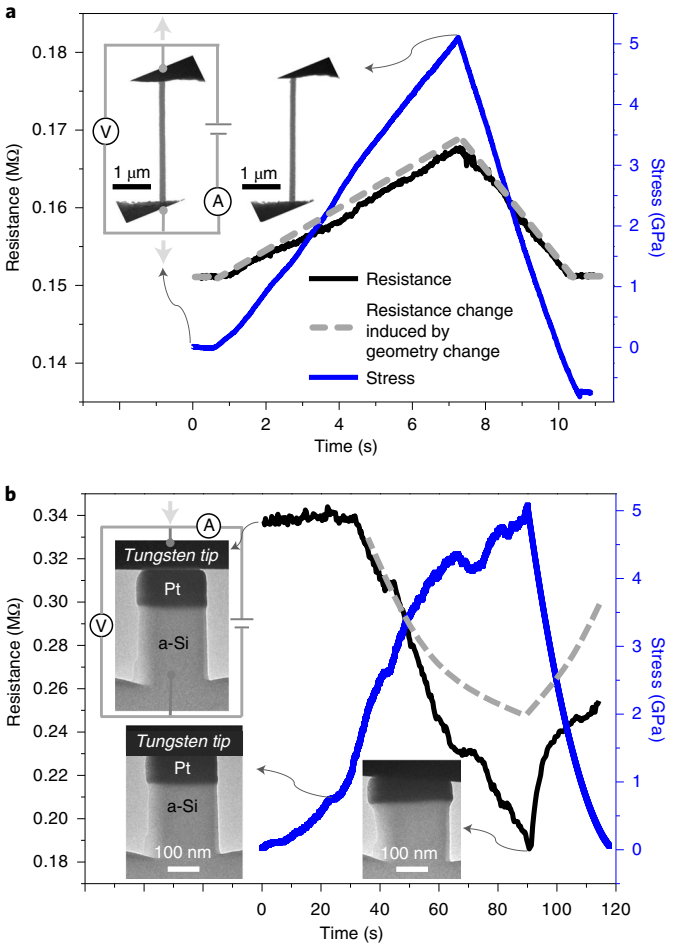

Fig. 4 | Electrical resistance measured for a-Si under tension versus compression. a, Stress excursion (blue curve) and corresponding resistance (black curve) as a function of time in the tensile test. The inset shows the experimental set-up and the tensile sample in its initial and final states. **b**, Stress excursion and corresponding resistance as a function of time in the compression test. The insets show the experimental set-up and the morphology of the compressed pillar at different states.

environments that are easier to further deform; the electrical resistance change in Fig. 4 provides credence to this mechanism, which becomes more prevalent with increasing plastic strain.

Specifically, the shear modulus G signifies the magnitude of the activation barrier Q for shear transformation events; the lower the G, the higher propensity for shear transformations[25], and vice versa. The normal-stress-sign-dependent G in a-Si thus goes hand in hand with the σ_n effect on Q, which can be described by the following:

$$Q = Q_0 - \tau\alpha_{\text{shear}}\Delta\epsilon_{\text{shear}}V_{\text{inital}} - \sigma_n\alpha_{\text{volume}}\Delta V \qquad (1)$$

where Q_0 is the energy barrier of a shear event at room temperature without applied stress, V_{initial} is the initial volume of the zone before transformation, and $\Delta\epsilon_{\text{shear}}$ and $\Delta V \equiv V_{\text{final}} - V_{\text{initial}}$ are the local shear strain and volume variation of the final configuration with respect to the initial configuration, respectively. The dimensionless quantities α_{shear} and α_{volume} describe the dependences of Q with respect to the shear stress τ and normal stress σ_n, respectively. If the elastic modulus does not depend on stress, α_{shear} and α_{volume} are simply the fraction of shear and dilation (or contraction) of the saddle-point configuration with respect to the entire (initial-to-final) transformation. But if it does, α_{shear} and α_{volume} would absorb that additional effect as well.

For a-Si, the elementary shear transformation event turns a relatively open structure into a contracted one[27,30,31]. In other words, a local cluster of atoms undergoes rearrangement from the relatively low-energy configuration to a metastable one, crossing a transition state with higher coordination number (Supplementary Fig. 15) and a volume reduction, as evidenced by the atomistic calculation of Boioli et al.[32]; with the supercell held fixed, they studied how the supercell pressure varies along the transition path: a negative pressure variation means a negative volume change (densification) of the transformation zone. As ΔV is negative for a-Si, and α_{volume} is a positive value, the sign of σ_n makes the difference observed in our experiment. Supplementary Fig. 16 schematically shows the resultant Q dependence on strain under tension and compression, reminiscent of the trends with the G_{xz} (or G_{yz}) evolution in Fig. 3d. The consequence is that compression lowers the shear modulus and the energy barrier, so the transition state is easier to be crossed, leading to easier pop-ups of shear transformation events. This instigates yielding at a lower stress, followed by strain softening (see the true stress–strain curve in Supplementary Fig. 17). By contrast, tension makes the shear events more difficult to be activated, such that the yield strength can reach a quite high value if flaw-induced premature fracture does not set in[7]. All in all, a-Si is stronger under tension but more 'ductile' under compression.

Importantly, such an extraordinary T-C asymmetry may exist in other amorphous materials with similar tetrahedral structures: $\sigma_C < \sigma_T$ is also found in our MD simulations of a-Ge and a-SiO_2 (silica glass; Supplementary Fig. 18). It could be a unique property

of open-framework covalently bonded glasses. For the metallic glass samples with similar dimensions, on the other hand, their σ_T is slightly lower than σ_C (Supplementary Fig. 19). This is because, unlike the open structure of a-Si (ref. [33]), metallic glasses are densely packed with CN on the order of 12 due to the non-directional metallic bonding[34], and their atomic shuffle in shear transformations causes volume expansion rather than shrinkage at the saddle point[35]. This distinction has a similar origin as the density anomaly in the melting of ice, which is lighter than liquid water, yet more shear-rigid and less diffusively mobile. The saddle-point states of the shear-diffusion transformation zone[36] by definition need to be less shear-rigid and more diffusively mobile than the starting state. Such a trend could be generic in tetrahedrally coordinated solids[37].

T-C asymmetry is critical for a-Si microelectronics or microelectromechanical systems devices that serve under T-C cyclic loading. The stress-sign-dependent modulus and energy barrier we proposed here, together with the strain-stiffening mechanism found in cementite, biological materials, elastomers[38] and so on, may inspire us to invent new materials with novel elastic properties. For small-scale a-Si devices, an unusually high yield strength and large yield strain may be desirable and can be achieved if the structural component is designed to be under tensile loading. Certainly, the higher tensile stress would eventually cause brittle failure. It has been reported that increasing hydrogen content will mitigate the brittleness in the tensile stress state[39–41]. Also, lithiated Si ($SiLi_x$) is of great application interest as an anode in a Li-ion battery. At a heavy degree of lithiation, the open-framework structure of silicon collapses, and the atomic structure is more akin to metallic glass. Correspondingly, it was found that a hydrostatic compressive stress strengthens the lithiated Si, while a hydrostatic tensile stress promotes its plasticity[42]. Therefore, it will be of interest to experimentally explore the chemical modulation of T-C asymmetry in a-Si.

Conclusion

In summary, through quantitative tension and compression testing of submicrometre-scale specimens, as well as detailed MD simulations, we have uncovered an extraordinary and pronounced T-C asymmetry in a-Si. First, the yield strength in tension is considerably higher than that in compression. The asymmetry in yield strength can be explained by the 'normal stress sign effect' on the shear moduli and thus activation energy barrier for the elementary shear events—shear transformations, which carry both the anelastic and plastic events. Compression lowers the activation barrier of shear transformations to facilitate yielding, whereas tension increases the activation barrier energy, rendering the activation of shear transformations more difficult and thus requiring a larger resolved shear stress. Second, in the nominally elastic regime, a hysteresis loop associated with the non-affine deformation appears only in compression. Third, the coupled mechanical–electrical tests revealing electrical resistivity changes have provided a sensitive indicator of the structural change underlying the T-C asymmetry: shear transformations have indeed been activated in compression but not in tension, switching semiconducting motifs to more metallic, denser, liquid-like ones. The asymmetry shown in this work is expected to hold for other materials similar to a-Si. In general, our findings provide insights for understanding the intrinsic response of open-framework glasses to different stress states. They may also be of practical relevance to the utility of small-scale a-Si in microelectronics and microelectromechanical systems.

Online content

Any methods, additional references, Nature Research reporting summaries, source data, extended data, supplementary information, acknowledgements, peer review information; details of author contributions and competing interests; and statements of data and code availability are available at https://doi.org/10.1038/s41563-021-01017-z.

Received: 14 January 2021; Accepted: 20 April 2021;
Published online: 31 May 2021

References

1. Meyers, M. A. & Chawla, K. K. *Mechanical Behavior of Materials* 2nd edn (Cambridge Univ. Press, 2008).
2. Chen, X., Wu, S. & Zhou, J. Influence of porosity on compressive and tensile strength of cement mortar. *Constr. Build. Mater.* **40**, 869–874 (2013).
3. Pelleg, J. *Mechanical Properties of Ceramics* Vol. 213 (Springer Science and Business, 2014).
4. Wachtman, J. B., Cannon, W. R. & Matthewson, M. J. *Mechanical Properties of Ceramics* (John Wiley and Sons, 2009).
5. Davidge, R. Mechanical properties of ceramic materials. *Contemp. Phys.* **10**, 105–124 (1969).
6. Griffith, A. The phenomena of flow and rupture in solids. *Phil. Trans. R. Soc. A* **221**, 163–198 (1920).
7. Zhao, P., Li, J. & Wang, Y. Extended defects, ideal strength and actual strengths of finite-sized metallic glasses. *Acta Mater.* **73**, 149–166 (2014).
8. Zhang, H. et al. Approaching the ideal elastic strain limit in silicon nanowires. *Sci. Adv.* **2**, e1501382 (2016).
9. Banerjee, A. et al. Ultralarge elastic deformation of nanoscale diamond. *Science* **360**, 300–302 (2018).
10. Tian, L. C. et al. Approaching the ideal elastic limit of metallic glasses. *Nat. Commun.* **3**, 609 (2012).
11. Hedler, A., Klaumünzer, S. L. & Wesch, W. Amorphous silicon exhibits a glass transition. *Nat. Mater.* **3**, 804–809 (2004).
12. Treacy, M. & Borisenko, K. B. The local structure of amorphous silicon. *Science* **335**, 950–953 (2012).
13. Wang, Y. et al. Tunable anelasticity in amorphous Si nanowires. *Nano Lett.* **20**, 449–455 (2020).
14. Sriraman, S., Agarwal, S., Aydil, E. S. & Maroudas, D. Mechanism of hydrogen-induced crystallization of amorphous silicon. *Nature* **418**, 62–65 (2002).
15. Deringer, V. L. B. et al. Origins of structural and electronic transitions in disordered silicon. *Nature* **589**, 59–64 (2021).
16. Gerbig, Y. B., Michaels, C. A., Bradby, J. E., Haberl, B. & Cook, R. F. *In situ* spectroscopic study of the plastic deformation of amorphous silicon under nonhydrostatic conditions induced by indentation. *Phys. Rev. B* **92**, 214110 (2015).
17. Liu, K., Ostadhassan, M., Bubach, B., Dietrich, R. & Rasouli, V. Nano-dynamic mechanical analysis (nano-DMA) of creep behavior of shales: Bakken case study. *J. Mater. Sci.* **53**, 4417–4432 (2018).
18. Ye, J. C., Lu, J., Liu, C. T., Wang, Q. & Yang, Y. Atomistic free-volume zones and inelastic deformation of metallic glasses. *Nat. Mater.* **9**, 619–623 (2010).
19. Herbert, E., Oliver, W. C. & Pharr, G. M. Nanoindentation and the dynamic characterization of viscoelastic solids. *J. Phys. D Appl. Phys.* **41**, 074021 (2008).
20. Yuan, Y. & Verma, R. Measuring microelastic properties of stratum comeum. *Colloids Surf. B* **48**, 6–12 (2006).
21. Stillinger, F. H. & Weber, T. A. Computer simulation of local order in condensed phases of silicon. *Phys. Rev. B* **31**, 5262–5271 (1985).
22. Justo, J. F., Bazant, M. Z., Kaxiras, E., Bulatov, V. V. & Yip, S. Interatomic potential for silicon defects and disordered phases. *Phys. Rev. B* **58**, 2539–2550 (1998).
23. Bartok, A. P., Kermode, J. R., Bernstein, N. & Csanyi, G. Machine learning a general-purpose interatomic potential for silicon. *Phys. Rev. X* **8**, 041048 (2018).
24. Deringer, V. L. et al. Realistic atomistic structure of amorphous silicon from machine-learning-driven molecular dynamics. *J. Phys. Chem. Lett.* **9**, 2879–2885 (2018).
25. Johnson, W. & Samwer, K. A universal criterion for plastic yielding of metallic glasses with a $(T/T_g)^{2/3}$ temperature dependence. *Phys. Rev. Lett.* **95**, 195501 (2005).
26. Fan, Z. & Ma, E. Predicting orientation-dependent plastic susceptibility from static structure in amorphous solids via deep learning. *Nat. Commun.* **12**, 1506 (2021).
27. Demkowicz, M. J. & Argon, A. S. High-density liquidlike component facilitates plastic flow in a model amorphous silicon system. *Phys. Rev. Lett.* **93**, 025505 (2004).
28. Rubinstein, M. & Panyukov, M. Nonaffine deformation and elasticity of polymer networks. *Macromolecules* **30**, 8036–8044 (1997).
29. Argon, A. & Demkowicz, M. What can plasticity of amorphous silicon tell us about plasticity of metallic glasses? *Metall. Mater. Trans. A* **39**, 1762–1778 (2008).

30. Demkowicz, M. J. & Argon, A. S. Liquidlike atomic environments act as plasticity carriers in amorphous silicon. *Phys. Rev. B* **72**, 245205 (2005).
31. Fan, Z., Ding, J., Li, Q. J. & Ma, E. Correlating the properties of amorphous silicon with its flexibility volume. *Phys. Rev. B* **95**, 144211 (2017).
32. Boioli, F., Albaret, T. & Rodney, D. Shear transformation distribution and activation in glasses at the atomic scale. *Phys. Rev. E* **95**, 033005 (2017).
33. Morishita, T. High density amorphous form and polyamorphic transformations of silicon. *Phys. Rev. Lett.* **93**, 055503 (2004).
34. Cheng, Y. & Ma, E. Atomic-level structure and structure–property relationship in metallic glasses. *Prog. Mater. Sci.* **56**, 379–473 (2011).
35. Schuh, C. A. & Lund, A. C. Atomistic basis for the plastic yield criterion of metallic glass. *Nat. Mater.* **2**, 449–452 (2003).
36. Li, W. et al. Deformation-driven diffusion and plastic flow in amorphous granular pillars. *Phys. Rev. E* **91**, 062212 (2015).
37. Daisenberger, D., McMillan, P. F. & Wilson, M. Crystal-liquid interfaces and phase relations in stable and metastable silicon at positive and negative pressure. *Phys. Rev. B* **82**, 214101 (2010).
38. Jiang, C. & Srinivasan, S. G. Unexpected strain-stiffening in crystalline solids. *Nature* **496**, 339–342 (2013).
39. Johlin, E. et al. Structural origins of intrinsic stress in amorphous silicon thin films. *Phys. Rev. B* **85**, 075202 (2012).
40. Gaire, C., Ye, D. X., Lu, T. M., Wang, G. C. & Picu, R. C. Deformation of amorphous silicon nanostructures subjected to monotonic and cyclic loading. *J. Mater. Res.* **23**, 328–335 (2008).
41. Abadias, G. et al. Review article: stress in thin films and coatings: current status, challenges, and prospects. *J. Vac. Sci. Technol. A* **36**, 020801 (2018).
42. Zhao, K. J., Li, Y. G. & Brassart, L. Pressure-sensitive plasticity of lithiated silicon in Li-ion batteries. *Acta Mech. Sin.* **29**, 379–387 (2013).

Publisher's note Springer Nature remains neutral with regard to jurisdictional claims in published maps and institutional affiliations.

© The Author(s), under exclusive licence to Springer Nature Limited 2021

Methods

Deposition of the a-Si film by plasma-enhanced chemical vapour deposition. For simplicity of the submicrometre-sized mechanical samples' preparation, a-Si film was deposited on a <001>-oriented and wedge-shaped single-crystalline Si substrate with an ~8 um top width (Supplementary Fig. 1a). An a-Si film was prepared using a plasma-enhanced chemical vapour deposition method with a radio frequency power of 20 W, at 250 °C substrate temperature, 800 mtorr process pressure, pure SiH_4 flow rate of 30 sccm and Ar flow rate of 475 sccm. The thickness of the a-Si film is about 11 µm. The deposited a-Si film adhered firmly to the substrate surface, and no obvious voids were found during the FIB milling process. The a-Si samples machined from the a-Si film have a uniform microstructure (Supplementary Fig. 1).

Sample preparation for nanomechanical tests. The a-Si pillars and tensile samples used in this work were microfabricated from the deposited parent body of a-Si film, using FIB (FEI Helios NanoLab 600 dual-beam FIB system) under a 30 kV accelerating voltage. The beam current of Ga ions sequentially decreased from 9.3 nA (coarse cutting) to 1.5 pA (fine polishing). Typical examples of the FIB-fabricated a-Si pillar and tensile samples (including the corresponding gripper, inset) are shown in Supplementary Fig. 3. The effective size d is defined as the nominal diameter measured at the half height of the pillars. The effective size d of the tensile samples is calculated by $d = \sqrt{A}$, where A is the measured cross-sectional area after brittle fracture.

In situ quantitative mechanical tests in TEM. The a-Si samples were compressed or tensioned under uniaxial loading performed by the Hysitron PI95 TEM PicoIndenter inside a JEOL JEM 2100F TEM instrument at 200 keV. The engineering stress was defined as the ratio of the measured load to the nominal cross-sectional area A of specimens, and the engineering strain ε was calculated to be the ratio of deformation displacement to the initial height h of pillars or initial length l of tensile samples. All in situ mechanical tests were carried out under the displacement control mode by changing the loading rate to keep a roughly constant strain rate for different samples. The strain rates for all tests were in the range $1\times10^{-3}\,s^{-1}$ to $5\times10^{-3}\,s^{-1}$ (quasi-static loading). The tensile and compressive tests were performed under comparable electron beam illumination.

Dynamic tensile and compressive tests. To ensure ultrahigh mechanical sensitivity in the dynamic tests, the Hysitron NanoIndenter system (Hysitron TI950) equipped with a nano dynamic mechanical analysis module, was employed. After calibration, the achievable resolutions of the nanoindentation system in displacement and in load are ~1 nm and ~1 µN, respectively. The a-Si pillars used for dynamic compressive tests were also fabricated by FIB in the same way as mentioned above. The tensile samples were lifted out from the prethinned a-Si lamellae using a piezoelectric micromanipulator (Kleindiek Nanotechnik) and then positioned on a microelectromechanical-systems-based push-to-pull device. The tensile sample was aligned carefully perpendicular to the trench edge to secure the uniaxial loading condition, and both ends were welded via ion-beam-induced Pt deposition. The whole process was performed inside a dual-beam FIB system (FEI Helios 600 NanoLab). To avoid fracture or plastic deformation, the nominal cyclic stress was set to be far less than the fracture strength or yield strength. To ensure the data reproducibility, ten loading cycles were applied for each run of the dynamic tests. The spectrum of each load cycle is of a triangular shape, consisting of symmetrical loading and unloading portions. It was found that ten loading cycles were sufficient to achieve a steady-state dynamic response in our present experimental set-up.

MD simulations. The a-Si model containing 8,192 atoms using ML potential was generated following a quench protocol similar to that in ref. [24], with sample dimensions of 4.5 nm × 4.3 nm × 8.7 nm in the x, y and z directions, respectively. Stress–strain curves for uniaxial tension and compression along the z direction were obtained from samples with free surface in the x direction and periodic boundary conditions in the y and z directions. All MD simulations were implemented in Large-scale Atomic/Molecular Massively Parallel Simulator (LAMMPS)[43]. The time step used in all simulations was 1 fs. ML-modelled a-Si was produced by heating a supercell of diamond silicon composed of $8\,(x)\times8\,(y)\times16\,(z)$ unit cells to 2,800 K into equilibrium liquid. Then it was quenched to 300 K with the effective cooling rate of $1\times10^{11}\,K\,s^{-1}$, following the similar protocol as that in ref. [24]. The a-Si samples using Stillinger–Weber and environment-dependent interatomic potentials contain 640,000 atoms and were prepared with the cooling rate of $1\times10^{12}\,K\,s^{-1}$. All those quenching and equilibrations were conducted in the isothermal-isobaric (NPT) ensemble under a Nose–Hoover thermostat with zero external pressure. The periodic boundary condition was applied in all three directions.

The deformation of a-Si samples was conducted at 300 K with the applied strain rate of $1\times10^{9}\,s^{-1}$ for the ML potential as well as $1\times10^{7}\,s^{-1}$ for the Stillinger–Weber and environment-dependent interatomic potentials. At different degrees of strain, the shear modulus G_{ij} along different orientations (that is, $\pm xy$, $\pm xz$ and $\pm yz$, and we use the average value of G_{+ij} and G_{-ij} as the value of G_{ij}) of the a-Si models was derived from the shear stress–strain curves at small (1.0%) strain. The vibrational mean squared displacement (MSD_i) of a single atom along the i direction is defined as $[x_i\,(t) - \bar{x}_i]^2$, where $\bar{x}_i$ is the equilibrium (time-averaged) position of the atom along the i direction, and the MSD is evaluated on short timescales when the MSD is flat with time and thus contains the vibrational but not the diffusional contribution[44]. The calculated MSD was taken by averaging over 100 independent runs, all starting from the same configuration but with momenta assigned randomly from the appropriate Maxwell–Boltzmann distribution.

Data availability

Source data are provided with this paper. Additional data reported in the Supplementary Information are available from the corresponding authors upon request.

Code availability

The computer codes are available from the corresponding authors upon reasonable request.

References

43. Plimpton, S. Fast parallel algorithms for short-range molecular dynamics. *J. Comput. Phys.* **117**, 1–19 (1995).
44. Ding, J. et al. Universal structural parameter to quantitatively predict metallic glass properties. *Nat. Commun.* **7**, 13733 (2016).

Acknowledgements

Z.S. and Y.W. acknowledge support from National Natural Science Foundation of China (51902249 and 5203000210), the National Key Research and Development Program of China (no. 2017YFB0702001) and China Postdoctoral Science Foundation (2019M663696). J.D. acknowledges support from National Natural Science Foundation of China (12004294) and National Youth Talents Program. J.L. acknowledges support by the National Science Foundation (DMR-1923976). L.T. acknowledges the Alexander von Humboldt Foundation and the Start-Bridge-Finish Program from International Center for Advanced Studies of Energy Conversion (ICASEC) for financial support. Z.F. thanks A. Bartok-Partay for the help in using the ML-based interatomic potential, and acknowledges the computational resources of the Maryland Advanced Research Computing Center. We thank R. Ritchie and M. Asta for helpful discussions. We thank J. Zhu, S. Yan and D. Zhang at Xi'an Jiaotong University for their assistance in nano dynamic mechanical analysis tests. E.M. and J.D. thank Xi'an Jiaotong University for supporting their work at the Center for Alloy Innovation and Design (CAID).

Author contributions

E.M., J.L. and Z.S. supervised the project. Y.W. and L.T. carried out the experimental investigations with assistance from M.L., H.L. and Y.Z.; J.D. and Z.F. led the modelling effort. E.M. and Y.W. wrote the paper with input from J.D., Z.F., J.L. and Z.S. All authors contributed to the discussions.

Competing interests

The authors declare no competing interests.

Additional information

Supplementary information The online version contains supplementary material available at https://doi.org/10.1038/s41563-021-01017-z.

Correspondence and requests for materials should be addressed to E.M., J.L. or Z.S.

Peer review information *Nature Materials* thanks Paul McMillan and the other, anonymous, reviewer(s) for their contribution to the peer review of this work.

Reprints and permissions information is available at www.nature.com/reprints.

nature portfolio

https://doi.org/10.1038/s41563-021-01017-z

Supplementary information

Tension–compression asymmetry in amorphous silicon

In the format provided by the authors and unedited

Supplementary Information

for

Tension-compression asymmetry in amorphous silicon

Yuecun Wang[1*], Jun Ding[2*], Zhao Fan[3*], Lin Tian[4*], Meng Li[1], Huanhuan Lu[1], Yongqiang Zhang[1], En Ma[2†], Ju Li[5†], Zhiwei Shan[1†]

[1]*Center for Advancing Materials Performance from the Nanoscale (CAMP-Nano) & Hysitron Applied Research Center in China (HARCC), State Key Laboratory for Mechanical Behavior of Materials, Xi'an Jiaotong University, Xi'an 710049, China*

[2]*Center for Alloy Innovation and Design (CAID), State Key Laboratory for Mechanical Behavior of Materials, Xi'an Jiaotong University, Xi'an 710049, China*

[3]*Department of Materials Science and Engineering, Johns Hopkins University, Baltimore, Maryland 21218, USA*

[4]*Institute of Materials Physics, University of Göttingen, Niedersachsen 37077, Germany*

[5]*Department of Nuclear Science and Engineering, and Department of Materials Science and Engineering, Massachusetts Institute of Technology, Cambridge, Massachusetts 02139, USA.*

This document contains Supplementary Figures (Fig. SI 1-19), Supplementary Notes (1-3), Supplementary Table and additional references (1-18).

Supplementary Video: *In-situ* TEM video shows the tension and compression processes of a representative a-Si TC sample.

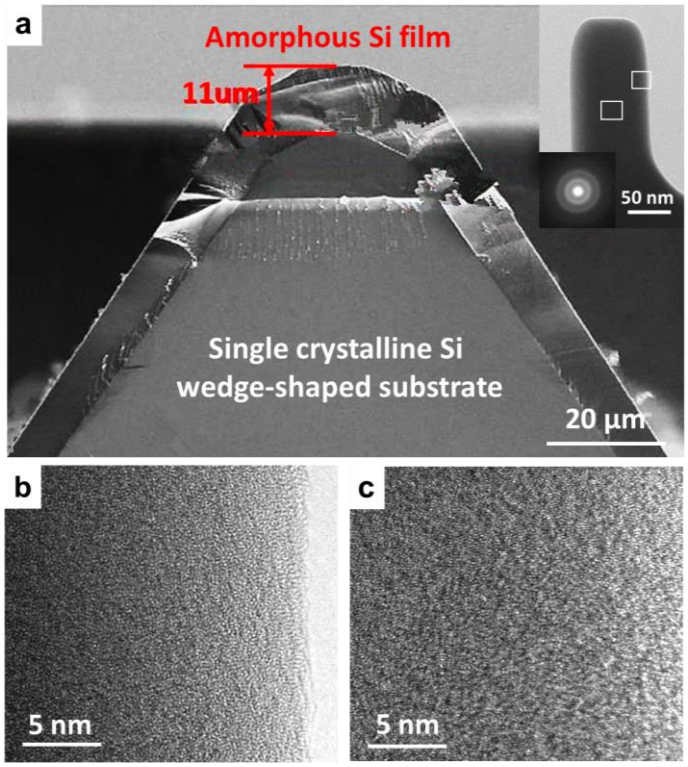

Fig. SI-1 | Sample information. (a) Cross-sectional SEM image of the deposited a-Si film on a wedge-shaped single-crystalline Si substrate. The thickness of the a-Si film (~11 μm) is large enough for fabricating the submicron-sized a-Si pillars using FIB. The inset shows the TEM image and electron diffraction pattern of an as-fabricated a-Si pillar. High-resolution TEM images of the white-boxed zones in the inset in (a), near the edge **(b)** and near the center **(c)** of the pillar. The diffraction halo and the maze-like feature of the phase-contrast in TEM images verify that the FIB-fabricated a-Si sample is fully amorphous without any visible crystalline phase.

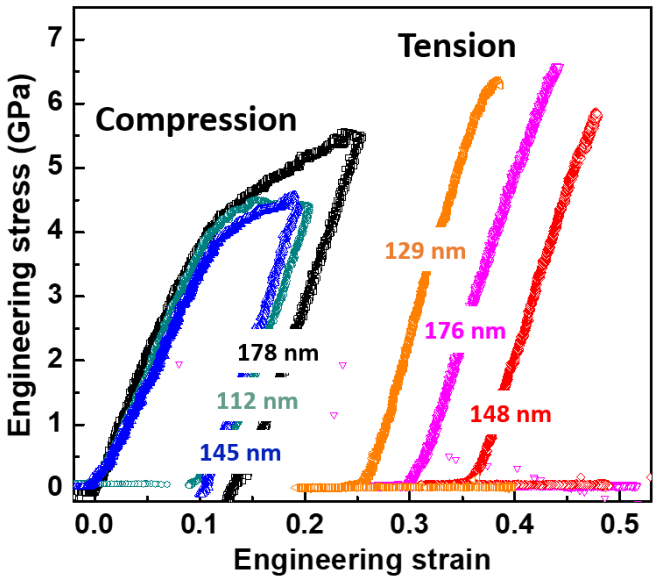

Fig. SI-2 | Typical engineering stress-strain curves of submicron a-Si pillars under compression (left) and dog-bone samples under tension (right).

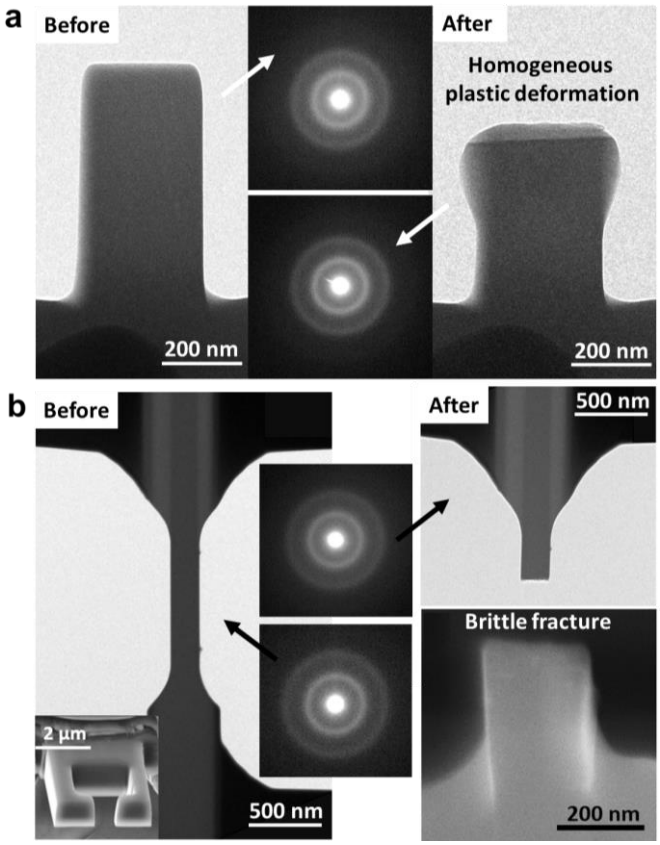

Fig. SI-3 | **(a)** TEM characterization of the FIB-fabricated a-Si pillar before (left) and after (right) compression. The mushroom-like morphology of the deformed a-Si pillar

indicates homogeneous plastic flow without shear-off. The halos in the diffraction pattern of the pillar indicate that there is no crystallization throughout the compression. **(b)** A prototypical "dog-bone" shaped tensile sample and its fracture surface. The flat fracture surface perpendicular to the tensile direction indicates that the fracture is brittle with little plastic deformation. The halos in the electron diffraction pattern of the fracture indicate that there is no crystallization.

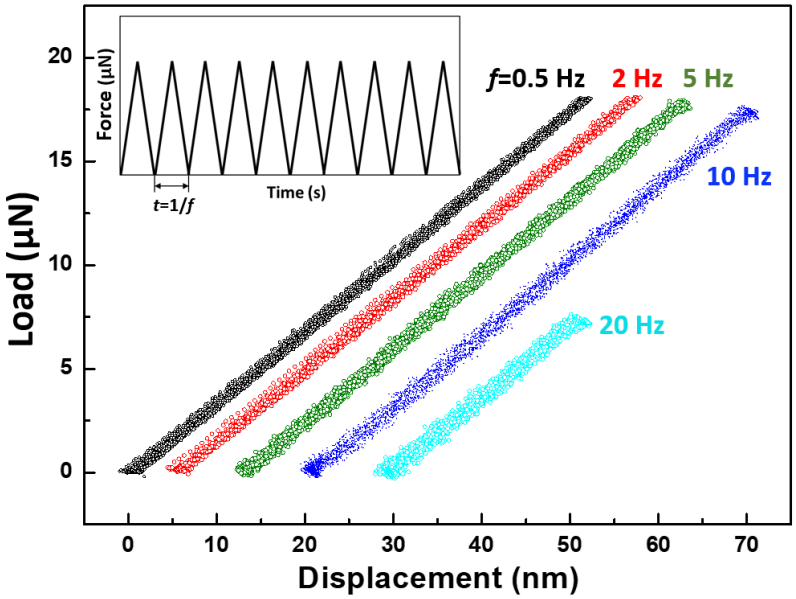

Fig. SI-4 | Load-displacement curves obtained by cycling an empty PTP device (without any samples) 10 times using the nano dynamic mechanical analysis (nano-DMA) technique. The dynamic tests were subsequently conducted with load control using a ~7 μm flat-end diamond punch. To ensure the data reproducibility, 10 loading cycles were applied for each run of the dynamic tests. The inset spectrum of each load cycle was of a triangular shape, consisting of symmetrical loading and unloading portions. The perfectly overlapped loading and unloading curves at different frequencies (0.5 Hz, 2 Hz, 5 Hz, 10 Hz and 20 Hz) indicate that the PTP device itself shows perfectly linear elasticity behavior under this condition.

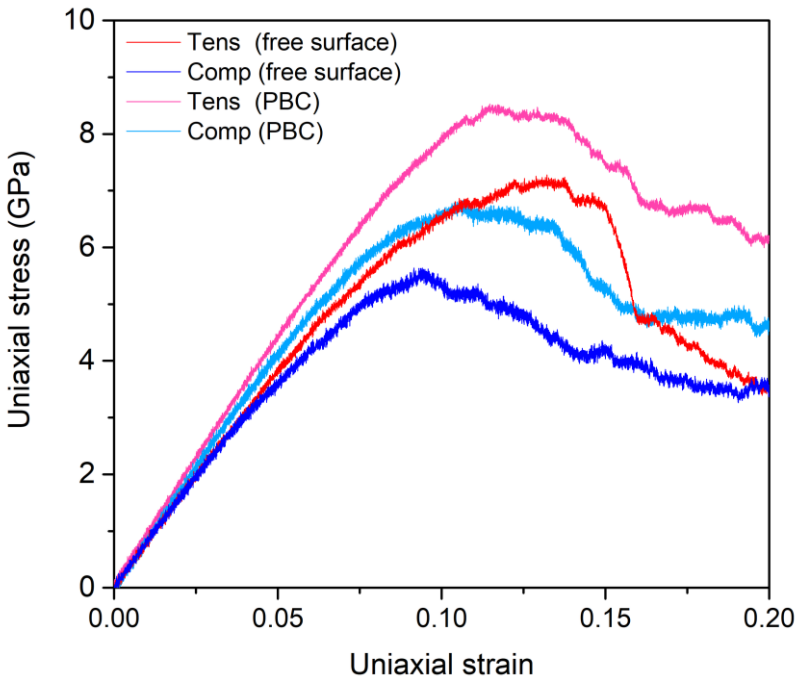

Fig. SI-5 | MD-simulated stress-strain curves for uniaxial tension and compression along *z* axis at 300 K, for ML a-Si model with and without free surface in the *x* direction, while *y* and *z* directions are under periodic boundary conditions (PBC).

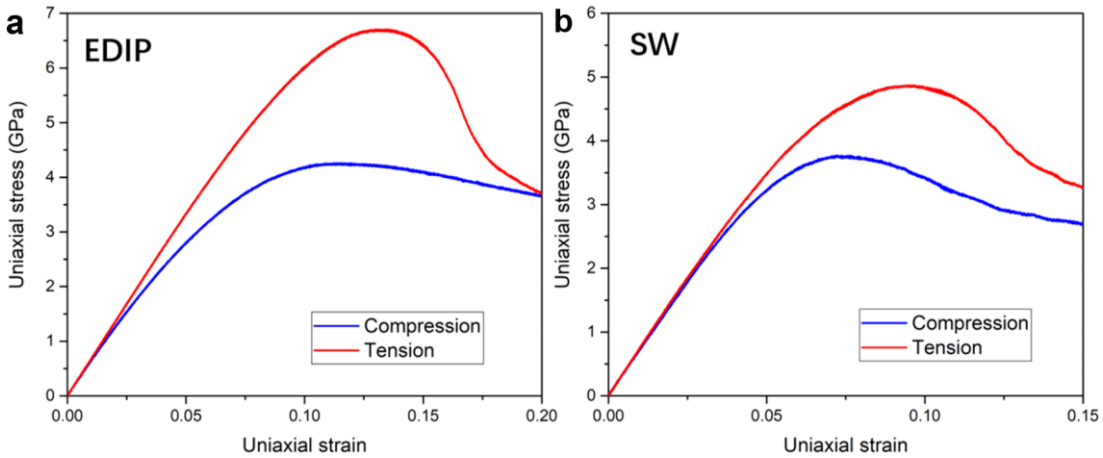

Fig. SI-6 | MD-simulated stress-strain curves for uniaxial tension and compression along *z*-axis at 300 K for a-Si pillars (with a diameter of 20 nm), using **(a)** EDIP and **(b)** SW potentials.

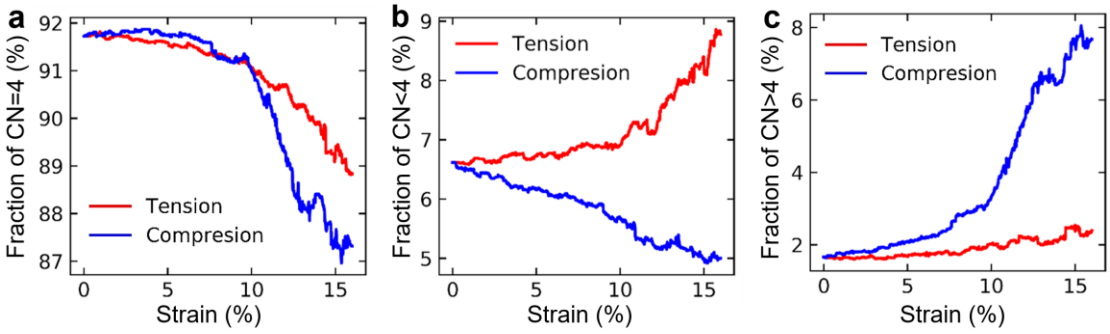

Fig. SI-7 | Evolutions of CN with tensile and compressive strains. Dependence of the fraction of a-Si atoms with CN=4 **(a)**, CN<4 **(b)** and CN>4 **(c)** on the tensile (red) and compressive (blue) strains, respectively. Note that some CN < 4 atoms are located close to the free surface.

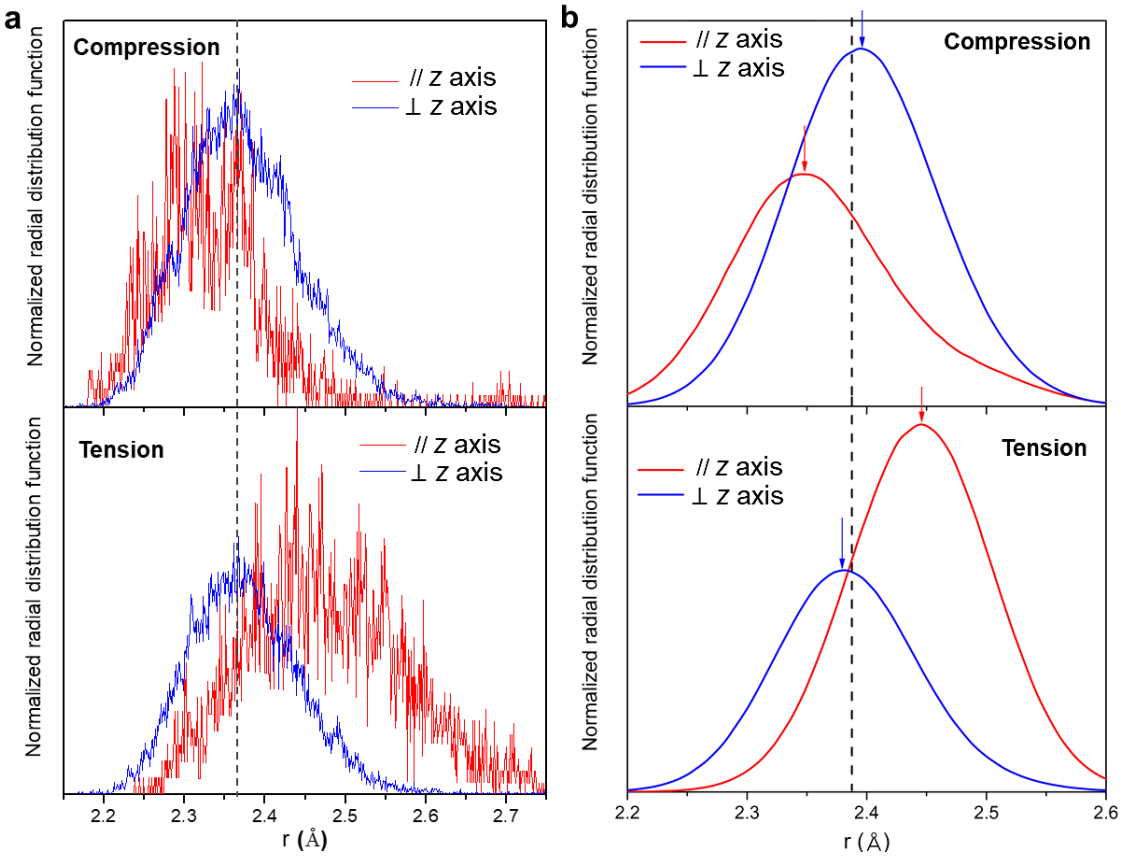

Fig. SI- 8 | Orientational radial distribution function (RDF) for the orientations parallel and perpendicular to *z* axis for the a-Si samples at the strain of 10% under compression & tension, simulated using ML potential **(a)** and EDIP potential **(b)**. The dashed line indicates the first peak position of the undeformed a-Si sample. The orientational RDF $g(r,\theta)$ is defined as $g(r,\theta) = \frac{1}{\kappa\rho N}\sum_{i=1}^{N}\sum_{j=1}^{N}\left[\delta(r-r_{ij})\cdot\delta\left(\theta-\theta_{\boldsymbol{z},\boldsymbol{r}_{ij}}\right)\right]$,

where $\theta_{\boldsymbol{z},\boldsymbol{r}_{ij}} = \arccos\left(\left|\hat{\boldsymbol{r}}_{ij} \cdot \hat{\boldsymbol{z}}\right|\right)$ is the angle between the z axis and the vector $\boldsymbol{r}_{ij}$, $\boldsymbol{r}_{ij}$ is the vector connecting a central atom i to a neighboring atom j, $r_{ij} = \left|\boldsymbol{r}_{ij}\right|$, ρ is the number density, N is the total number of atoms in a sample, $\kappa = 4\pi r^2 \Delta r[\cos(\theta - 0.5\Delta\theta) - \cos(\theta + 0.5\Delta\theta)]$, and here we use $\Delta\theta = 10^{\circ}$. For clarity, we only contrast $g(r,\theta)$ curves at two extreme ends, i.e. $\theta = 5^{\circ}$ (// z axis) and $\theta = 85^{\circ}$ ($\perp$ z axis), in these plots. The a-Si samples simulated using EDIP potential contain over 1 million atoms, about twenty times larger than those simulated using ML potential. The latter can only be applied for much smaller samples due to its extremely high computation cost; due to the small sample size and associated noise in the data, it is difficult to confirm the first peak shift for the orientation perpendicular to z-axis under compression versus tension (a). The bigger samples producing smooth curves (see b) are therefore useful: the peak shift now becomes readily observable (see the arrow pointing to the shifted peak).

Supplementary Note 1:

In addition to the normal stress sign dependent shear moduli, we consider two previously known structural excursions in a-Si under stress/pressure. One is the polyamorphic phase transition, which transforms the low-density amorphous (LDA) state to the high-density amorphous (HDA) state, as demonstrated in previous studies[1,2]. But this polyamorphism requires an externally applied hydrostatic pressure as high as ~12-14 GP in experiments and >10 GPa in our MD simulation (Fig. SI-9). Such a magnitude is considerably higher than the compressive yield strength observed in our study. We can therefore rule out the LDA-HDA transformation as relevant to our T-C asymmetry. The other structural change is deformation-induced fertile sites for shear transformations, such as the increase of denser fivefold-coordinated liquid-like motifs converted from fourfold-coordinated solid-like ones[3,4]. However, this alone cannot explain the T-C asymmetry of a-Si, and especially the softening even at small strains. First, as clearly presented in Fig. 3d, the shear moduli have undergone noticeable

changes as early as in the nominally elastic regime, where the content of deformation-created liquid-like regions should be very low. Second, G_{xz} (or G_{yz}) can even be increased rather than decreased upon straining when $\sigma_n > 0$. Third, the fraction of atoms with CN > 4 remains rather limited throughout the deformation (Fig. SI-7). Therefore, the normal stress effect observed, especially in the early stage of deformation, cannot be accounted for solely by fertile sites created by shear transformations. Instead, two main factors are contributing to the T-C asymmetry. One is the above plasticity-induced fertile sites (softening), which becomes more important at large normal stress/strain (i.e., beyond elastic regime). The other factor is the anisotropic evolution of the shear moduli due to the imposed normal stress (see main text), starting from the early stage of deformation. With increasing $\sigma_n > 0$ (tension), the modulus initially increases as the atomic arrangement evolves, but eventually decreases at large normal stress when activated shear transformations take over to convert many tetrahedral solid-like atomic environments into liquid-like fertile sites[3,5,6]. In comparison, at $\sigma_n < 0$ (compression), both of these two factors contribute to softening, thus leading to decreasing shear moduli with strain in a fast and monotonic manner.

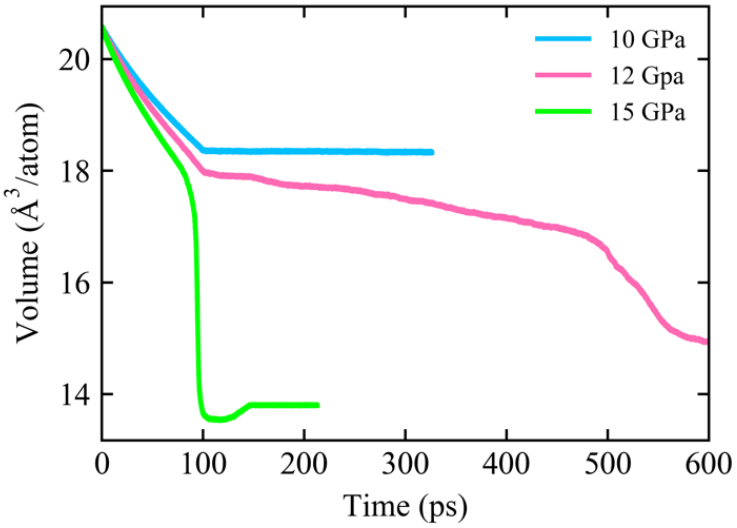

Fig. SI-9 | The average atomic volume of ML modeled a-Si as a function of relaxation time under various hydrostatic pressure at 300 K. The hydrostatic pressure is increased at constant rate to target pressure during the first 100 ps and then kept constant.

In previous work, we have developed the flexibility volume parameter[7,8],

combining mean squared displacement (MSD) and atomic volume, allowing universal prediction of G in metallic glass and a-Si at different compositions and cooling history. However, for the current case of a-Si under normal stress, G is no longer isotropic, and neither is the MSD. For example, as shown in Fig. SI-10a and 10b, MSD_z (MSD in z direction) is not equal to MSD_x or MSD_y (MSD_x=MSD_y) under different normal stress in z direction. We therefore modify the previous definition to define an orientational flexibility volume parameter λ_{ij},

$$\lambda_{ij}=0.5\times(\mathrm{MSD}_i+\mathrm{MSD}_j)\times r\cdot\frac{(1+\varepsilon_k)}{(1+\varepsilon_j)} \tag{S1}$$

where $i, j, k \in x, y$ or z directions, r is the average atomic spacing, ε_k and ε_j are the strain along k and j, respectively, after applying a normal stress. As demonstrated in Fig. SI-10c (also Fig. SI-11), G_{ij} of a-Si at different normal strains correlates very well with the inverse of λ_{ij}, suggesting that orientational flexibility volume is an effective structural parameter to characterize the mechanical property of amorphous materials.

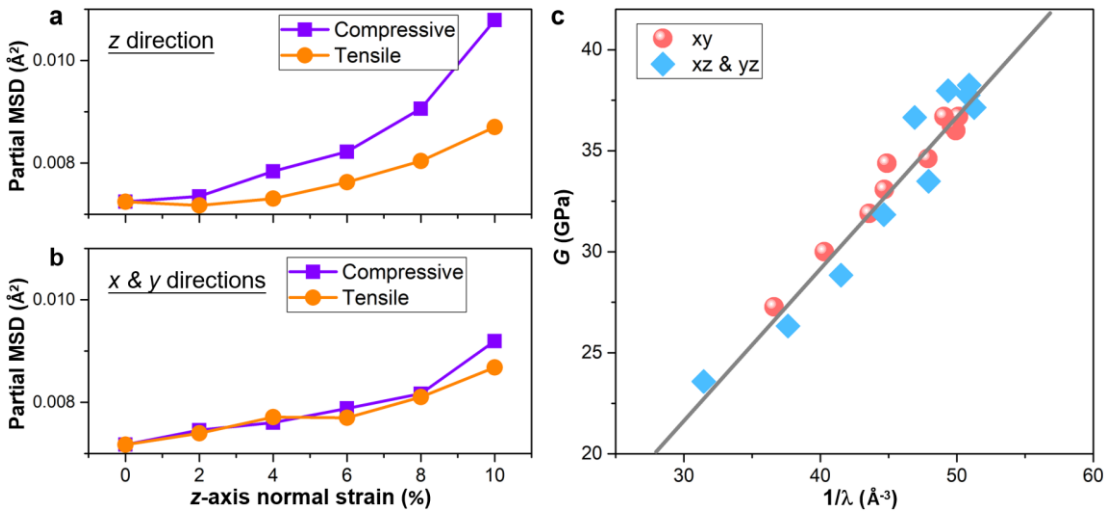

Fig. SI-10 | Orientational flexibility volume parameter λ_{ij} unifying the anisotropic shear moduli at different normal stress. The anisotropic MSD for **(a)** z-direction and **(b)** x or y directions when the ML a-Si model reaches different z-axis normal strains. **(c)** Correlation between the shear moduli G_{ij} and the inverse of the corresponding orientational flexibility volume. The straight line serves as a guide to the eye.

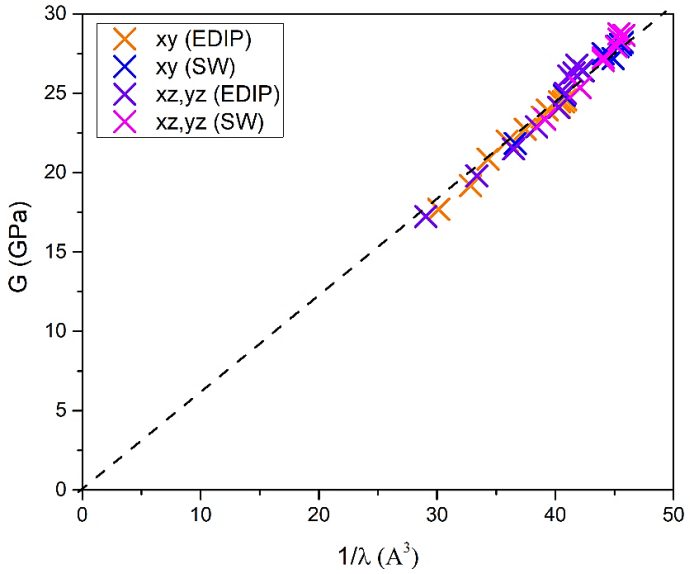

Fig. SI-11 | A strong correlation is observed between the shear moduli G_{ij} and the inverse of the corresponding orientational flexibility volume, for MD-simulated a-Si using SW and EDIP potentials. The straight dash line serves as a guide to the eye.

Supplementary Note 2: *In-situ* coupled mechanical-electrical tests for the resistance measurement

Resistance measurement under tensile strain:

A-Si tensile sample was transferred to an electrical PTP (E-PTP) device, and both ends of the sample were welded on Au electrodes. More details about the E-PTP device can be found in reference[9]. The E-PTE devices matches with the Hysitron PI95 ECR TEM holder. The coupled mechanical-electrical test was performed inside TEM (JEOL 2100F, 200 kV). Firstly, the I-V curve was obtained by sweeping the voltage (V) from -0.1 V to 0.1 V and recording the electrical current (I) simultaneously. The linear I-V curve indicates the perfect Ohmic contact (Fig.SI-12a), and the resistance can be directly calculated with Ohm's law. Subsequently, a constant voltage of 100 mV was applied on the a-Si sample which is loaded via the diamond punch pushing the movable end of E-PTP, and meanwhile the current through the sample can be measured.

Resistance measurement under compressive strain:

The Si wedge with a-Si pillar on its top was glued on a conductive copper sample mount using the conductive epoxy. The copper mount is screwed on one end of the ECR holder, and the other end of the holder is a conductive tungsten punch used for forming the circuit when touching the sample. In order to ensure the Ohmic contact (the linear relationship between voltage and current, Fig. SI-12b) and to avoid the localized deformation of a-Si induced by contact effect of the tip and pillar, the top of a-Si pillars was covered with a Pt cap during FIB fabrication. A constant voltage was applied upon the touch of W tip with pillar, and then the corresponding current was measured during compression.

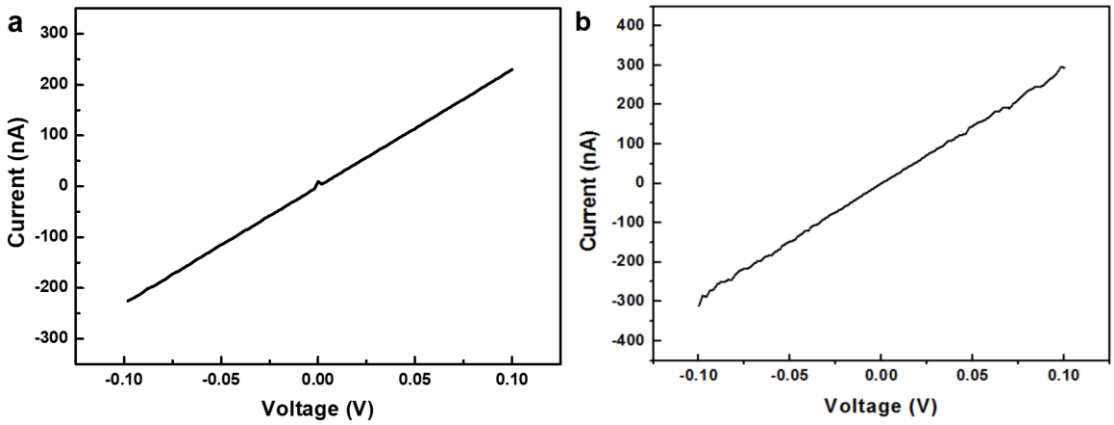

Fig. SI-12 | *I-V* curves were obtained by sweeping the voltage (*V*) from -0.1 V to 0.1 V and recording the electrical current (*I*), for mechanical-electrical coupling tests in tension **(a)** and compression **(b)**. The linear *I-V* curve indicates perfect Ohmic contact, and the resistance can therefore be calculated using Ohm's law.

Calculation of resistance change caused by geometry change under straining:

The sample resistance (*R*) is given by

$$R = \rho L / S \tag{S2}$$

where ρ is the resistivity, L and S are the length and cross-sectional area of the sample, respectively. The sample volume $V=S\times L$ is expected to be constant during the

homogeneous flow. At strain x, the length of a-Si under tension

$$L|_{(strain=x)} = L_0(1+x) \tag{S3}$$

where L_0 is the initial length. As such, the resistance at strain x can be evaluated as

$$R|_{(strain=x)} = (\rho(L|_{(strain=x)})^2)/V = (L_0{}^2(1+x)^2)/V = R_0(1+x)^2 \tag{S4}$$

where R_0 is the initial resistance.

Table S1 lists the a-Si samples information about their dimensions, initial resistances, the calculated and measured resistance changes under tension and compression, respectively.

Table S1. Sample dimensions and resistances change of a-Si under tension and compression

Sample	Diameter (nm)	Length (nm)	Initial Resistance (MΩ)	Resistance (Geometry change induced) (MΩ)	Resistance (at max strain) (MΩ)	Resistance (after unloading) (MΩ)
Tensile sample	188	3800	0.152	0.166	0.164	0.155
Pillar	200	310	0.342	0.248	0.186	0.253

The grey dashed line in Fig. 4a (in the main text) shows the resistance calculated using Eq. (S4) as a function of time (tensile strain). The curve agrees well with the measured resistance, indicating that the observed resistance increase during tensile deformation arises entirely from geometry change, and the resistivity stays constant.

This is no longer the case in the compression test, where resistance decreased from the initial 0.342 MΩ to 0.186 MΩ when the compressive strain reached -14.8% (see Fig. 4b in the main text). Upon unloading, the resistance of the pillar rose but only back to 0.253 MΩ after the sample was detached from the tungsten tip. The plastic strain of a-Si (measured from snapshots from the *in-situ* video) is about -5%, and the calculated resistance after unloading is 0.308 MΩ, higher than the measured resistance (0.253 MΩ). Given the resistivity of the deposited Pt cap is three orders of magnitude lower than that of the a-Si pillar [10] and that the size of the base beneath the pillar is very large,

the measured resistance should mainly come from the a-Si pillar. Besides, we also rule out the contribution from the elastic strain filed in the a-Si to the measured resistance change in our mechanical-electrical coupling experiment setup (Fig. SI-13).

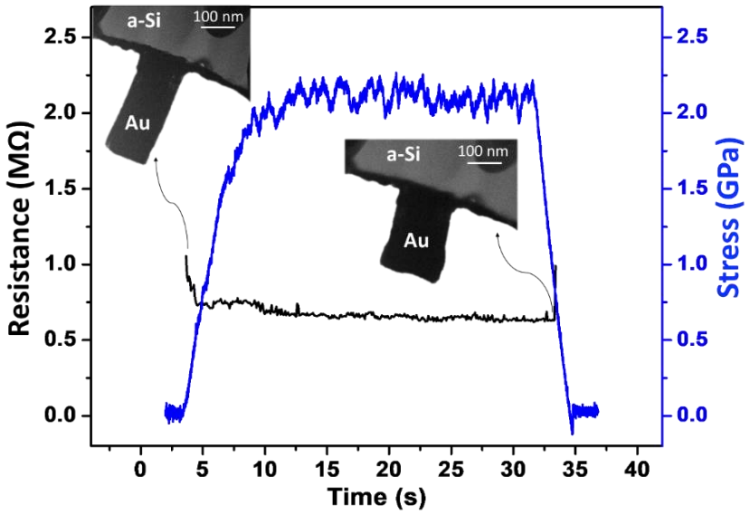

Fig. SI-13 | Electrical resistance measurement of the a-Si base beneath the FIB-fabricated Au pillar. Soft Au film was deposited on a-Si, and then micromachined using FIB into pillar shape to form Ohmic contact with the tungsten tip. During the compression of the Au pillar, which has a low resistance that can be ignored compared with that of a-Si, the measured resistance stayed almost unchanged. This suggests that in our mechanical-electrical coupling experiment setup the elastic strain filed in the a-Si base has no contribution to the measured resistance change, which mainly comes from the geometry and resistivity of a-Si pillar under compression.

Supplementary Note 3: the plasmon energy E_p maps representing the (electron) density distributions of a-Si under tension and compression

In order to study the effect of tensile and compressive deformation on structure changes in a-Si, volume plasmon energy E_p maps were collected in a bent a-Si pillar on both its tensile side and compression zones[11]. As mentioned in the main text, the transformation from the tetrahedral solid-like (lower-density) state to the denser

fivefold liquid-like one is a crucial factor in the plastic deformation of a-Si. Therefore, it is important to measure the density difference between the tensioned and compressed a-Si for evaluating the structural change under tension and compression.

We performed electron energy loss spectroscopy (EELS) mapping on a bent a-Si pillar with a diameter of ~50 nm (Fig. SI-14a) to obtain the density distributions in the tension and compression zones by measuring the volume plasmon energy E_p, which was successfully used previously to obtain the mass density of a-Si films[12]. Based on the free-electron assumption, the plasmon energy E_p is given by[13]:

$$E_p = \hbar\left(\frac{n_e e^2}{\varepsilon_0 m^*}\right)^{1/2} \quad \text{(S5)}$$

where n_e is the number density of valence electron, $\hbar$ is the reduced Planck's constant, e is electron charge, m^* is the mass of electron, and ε_0 is dielectric constant of the vacuum. E_p, which is proportional to the square root of the number density of valence electrons (also the number density of Si atoms if we assume the total number of electrons in the sample does not change), can be directly obtained from the EELS spectrum. The EELS data were acquired in a JEOL JEM-2100F STEM equipped with a Gatan Quantum 963 GIF. Standard imaging conditions have an accelerating voltage of 200 kV, a 40 μm diameter condenser aperture, and an electron beam probe size of 0.2 nm. To determine the E_p of a-Si with high precision, we fit with Gaussians both the zero-loss peak and the first plasmon peak intensities in the EELS spectrum captured at each STEM raster. The two peaks are overlapped, the difference between the central energy of each peak is taken to be the energy loss E_p induced by plasmon oscillations. To determine the center energy of the zero loss peak and plasmon peak we used the method introduced in reference [14]. Each map contains 10×10 pixels on a 0.65 nm pitch. Repeated measurements at a single point give standard deviations in the E_p value of 15 meV~80 meV. As shown in Fig. SI-14, the compressively strained side shows much higher E_p and therefore larger valence electron density, compared with tension side. Furthermore, E_p mapping from the compression side shows larger heterogeneity with some local high E_p regions. According to Eq. (S5), we can get $n_e / n_e' = (E_p / E_p')^2$. The

maximum E_P measured in the compression side is 19.2 eV, and the average E_p' measured from the tension side is 16.9 eV. The corresponding n_e has an increase of 25%. This increase is consistent with the conjecture that in local regions the coordination number increases from ~4 (solid-like) to ~5 (liquid-like), also a 25% increase.

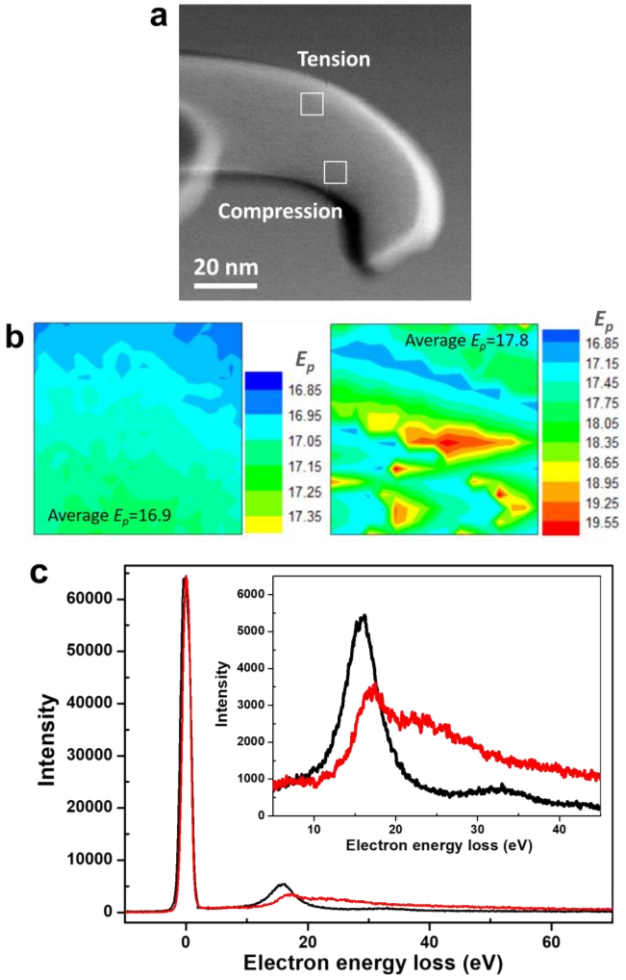

Fig. SI-14 | Quantitative EELS was used to investigate the density difference between the compressive side and tensile side of a bent a-Si pillar with the original diameter d = ~ 50 nm inside TEM. **(a)** STEM image of the bent a-Si pillar. **(b)** 2D contour image showing the plasmon energy E_p maps on the tension (left) and compression (right) zones marked by the white frames in (a). The compression side shows much higher E_p and therefore larger electron density, compared with the tension side. Furthermore, E_p mapping from the compression side shows larger heterogeneity with some local high E_p regions. This indicates that more liquid-like regions form as plasticity carriers under

compression, while the transformation from lower density to higher density is suppressed under tension. **(c)** The typical low-loss EELS spectra of E_p=17 eV (black) and E_p=19 eV (red) with the zero-loss peaks overlapped. The inset shows their enlarged plasmon peaks with different shapes and positions, and they correspond to the solid-like and liquid-like regions, respectively.

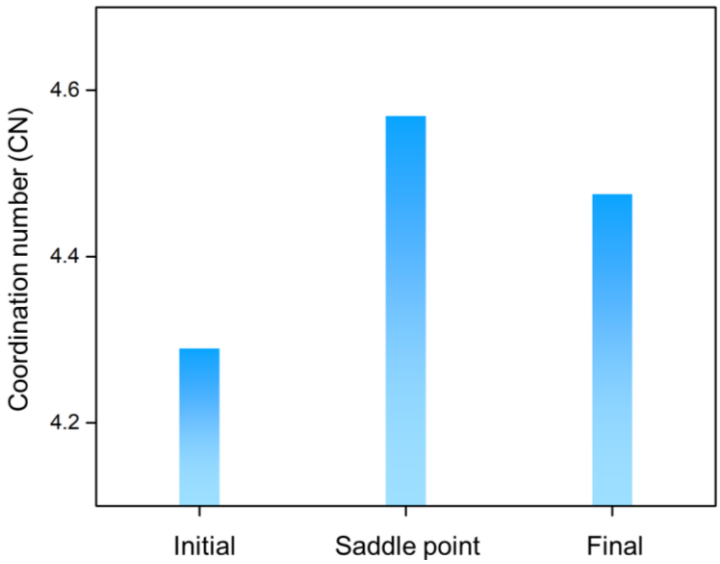

Fig. SI-15 | Average coordination number for initial, saddle and final state of a-Si calculated using SW potential. The search of saddle and final states of thermal activation events was performed using activation-relaxation technique (ART) package. Initial perturbations in ART were introduced by applying random displacement on a small group of atoms (an atom and its nearest-neighbors)[15,16]. The magnitude of the displacement was fixed, while the direction was randomly chosen. When the curvature of the potential energy landscape was found to overcome the chosen threshold, the system was pushed towards the saddle point using the Lanczos algorithm. The saddle point is considered to be found when the overall force of the total system is below 0.01 eV/Å. The corresponding coordination number of centered Si atoms was determined by the distance cutoff using the position of first minimum in pair distribution functions.

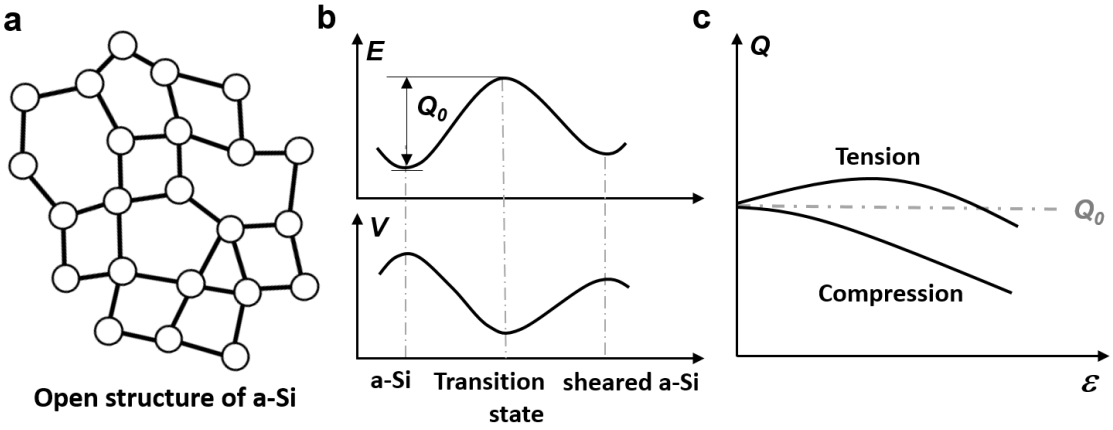

Fig. SI-16 | Schematic illustrating the normal-stress-sign-dependent activation barrier *Q* for shear transformation events. (a) Schematic showing the open network structure of the unstrained a-Si. **(b)** The energy E, as well as volume V [17] (also see Fig. SI-15 above), of a-Si in a shear deformation event, from the relatively low energy configuration to a metastable sheared configuration, crossing a transition state (saddle-point configuration) of higher energy and density. **(c)** Activation energy barrier Q as a function of strain ε under tension and compression, respectively, showing similar trends with the G change in Fig. 3d.

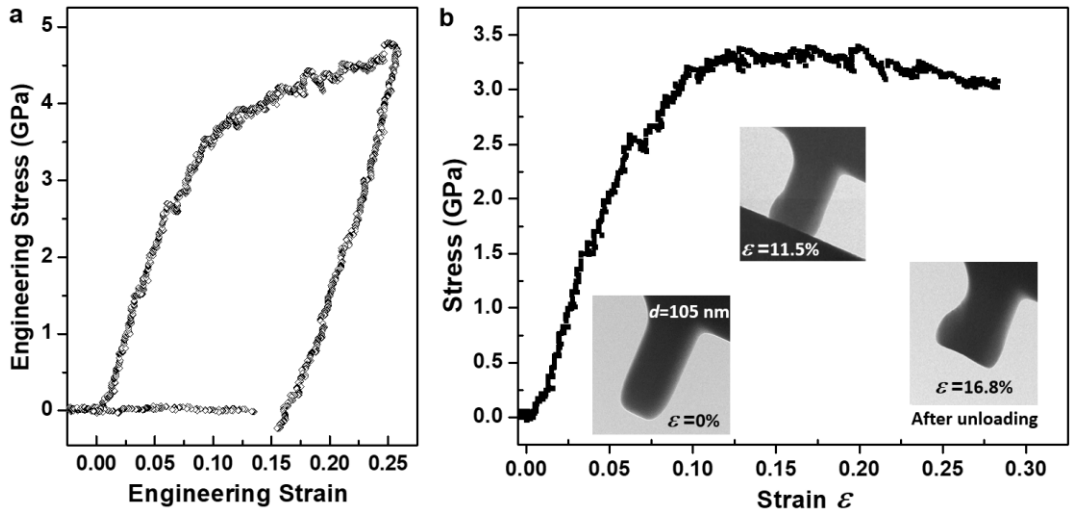

Fig. SI-17 | (a) Engineering stress-strain curve of an a-Si pillar with effective size d=105 nm. **(b)** True stress-strain curve of the pillar. The true stress was calculated by dividing the deformed pillar's top area by the applied load. The insets show the morphology evolution of the a-Si pillar under compression.

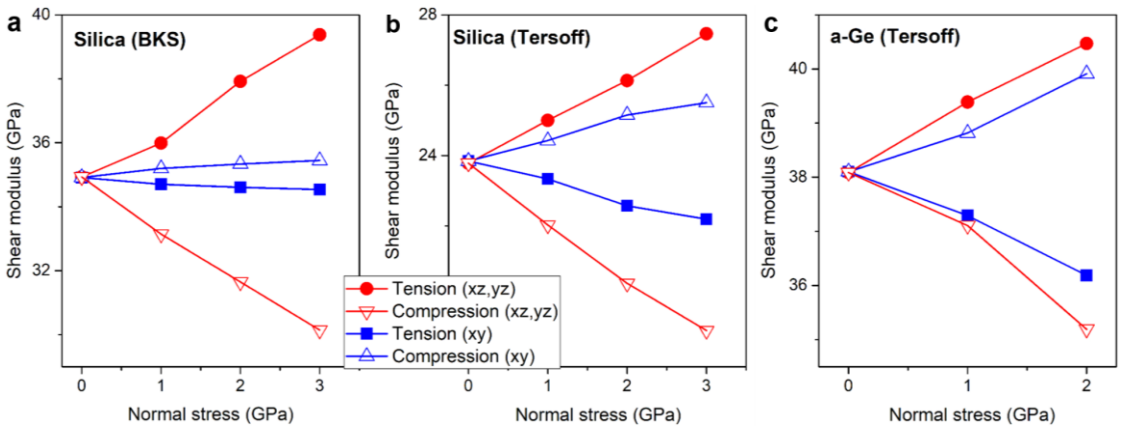

Fig. SI-18 | Effects of normal stress (σ_n in z direction) on the shear moduli G_{xz} (or G_{yz}) and G_{xy} of **(a)** silica using BKS potential[18], **(b)** silica using Tersoff potential and **(c)** amorphous Ge using Tersoff potential.

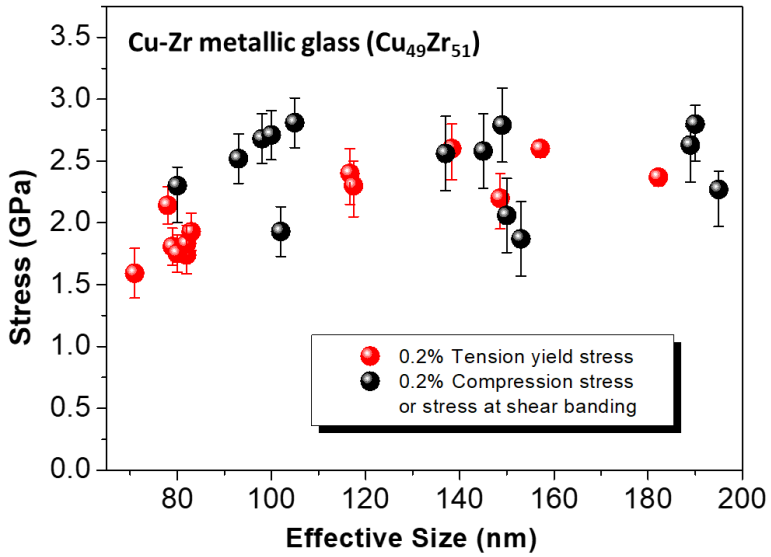

Fig. SI-19 | Yield strength in tension versus compression, for submicron samples of a Cu-Zr metallic glass, showing only slight tension-compression asymmetry, with σ_C a little higher than σ_T.

Supplementary References

1. Shimomura, O. *et al.* Pressure-induced semiconductor-metal transitions in amorphous Si and Ge. *Philos. Mag.* **29**, 547-558 (1974).
2. Daisenberger, D., *et al*. Polyamorphic amorphous silicon at high pressure: raman and spatially resolved

X-ray scattering and molecular dynamics studies. *J. Phys. Chem. B.* **115**, 14246-14255, (2011).
3. Demkowicz, M. J. & Argon, A. S. High-density liquidlike component facilitates plastic flow in a model amorphous silicon system. *Phys. Rev. Lett.* **93**, 025505 (2004).
4. Gerbig, Y. B., Michaels, C. A., Bradby, J. E., Haberl, B. & Cook, R. F. In situ spectroscopic study of the plastic deformation of amorphous silicon under nonhydrostatic conditions induced by indentation. *Phys. Rev. B* **92**, 214110 (2015).
5. Argon, A. S., & Demkowicz, M. J. What can plasticity of amorphous silicon tell us about plasticity of metallic glasses? *Metall. Mater. Trans. A* **39**, 1762-1778 (2008).
6. Demkowicz, M. J. & Argon, A. S. Liquidlike atomic environments act as plasticity carriers in amorphous silicon. *Phys. Rev. B* **72**, 245205 (2005).
7. Fan, Z., Ding, J., Li, Q. J., Ma, E. Correlating the properties of amorphous silicon with its flexibility volume. *Phys. Rev. B* **95** (2017).
8. Ding, J., Cheng, Y. Q., Sheng, H., Asta, M., Ritchie, R O, Ma, E. Universal structural parameter to quantitatively predict metallic glass properties. *Nature Commun.* **7**, 13733 (2016).
9. Wang, X. *et al.* Growth conditions control the elastic and electrical properties of ZnO nanowires. *Nano Lett.* **15**, 7886-7892 (2015).
10. Langford, R. M., Wang, T. X. & Ozkaya, D. Reducing the resistivity of electron and ion beam assisted deposited Pt. *Microelectron. Eng.* **84**, 784-788 (2007).
11. Wang, Y., Liang, B., Xu, S., Tian, L., Minor, A. M., Shan, Z. Tunable anelasticity in amorphous Si nanowires. *Nano Lett.* **20**, 449-455 (2020).
12. Haberl, B. *Structural characterization of amorphous silicon* Doctor of Philosophy thesis, The Australian National University, (2010).
13. Egerton, R. F. *Electron energy-loss spectroscopy in the electron microscope*. Springer Science & Business Media, (2011).
14. Mecklenburg, M. *et al.* Nanoscale temperature mapping in operating microelectronic devices. *Science* **347**, 629-632 (2015).
15. Barkema, G. T., Mousseau, N. Event-based relaxation of continuous disordered systems. *Phys. Rev. Lett.* **77**, 4358–4361 (1996).
16. Rodney, D., & Schuh, C. Distribution of thermally activated plastic events in a flowing glass. *Phys. Rev. Lett.* **102**, 235503 (2009).
17. Boioli, F., Albaret, T., Rodney, D. Shear transformation distribution and activation in glasses at the atomic scale. *Phys. Rev. E* **95**, 033005 (2017).
18. Kramer, G. J., Farragher, N. P., Van Beest, B. W. H., & Van Santen, R. A. Interatomic force fields for silicas, aluminophosphates, and zeolites: derivation based on ab initio calculations. *Phys. Rev. B* **43**, 5068 (1991).